

Observations and analysis of an urban boundary layer during extreme heat events

Gabriel Rios ^{1*}, ^{2*}, Prathap Ramamurthy ^{1, 2}

1. Department of Mechanical Engineering, CUNY City College, New York, New York

2. NOAA Center for Earth System Sciences and Remote Sensing Technologies, New York, New York

Corresponding author: Gabriel Rios (grios001@citymail.cuny.edu)

*** Current affiliation(s):** Department of Mechanical Engineering, CUNY City College, New York, New York; NOAA Center for Earth System Sciences and Remote Sensing Technologies, New York, New York

For submission to the Quarterly Journal of the Royal Meteorological Society.

Last updated: February 11, 2022.

¹ Abstract

Extreme heat presents a significant risk to human health and infrastructure in cities. Several studies have been conducted in the past two decades to understand the interaction between the synoptic-scale extreme heat events and local-scale urban heat island effects. However, observations of boundary layer characteristics during these periods have been relatively rare. Our current understanding of boundary layer dynamics is incomplete, particularly in coastal urban environments where the local climatology is highly influenced by land-sea thermal gradients. Here we analyze the evolution and structure of the urban boundary layer during regular and extreme heat periods. Our primary goal is to understand how boundary layer dynamics during extreme heat events regulate near-surface transport of mass, momentum, and heat. The analysis will also focus on how the urban surface layer interacts with the mixed layer during these events. Our analysis focuses on the New York City metropolitan area and relies on observations from vertical profilers (Doppler lidar, microwave radiometer) and quantities derived by analytical methods. Additionally, satellite and reanalysis data are used to supplement observational data.

¹⁴ 1 Introduction

Extreme heat poses a major risk to life and property. The effects of extreme heat are expected to impact cities especially, which presents a significant hazard for vulnerable populations and infrastructure. With regards to effects on public health, studies have shown that extreme and prolonged heat increases mortality and exacerbates existing health conditions in high-risk populations (Anderson and Bell, [2011](#); Frumkin, [2016](#); Heaviside, Macintyre, and Vardoulakis, [2017](#); Madrigano et al., [2015](#)). With regards to effects on infrastructure, studies have shown that extreme heat subjects networks critical to urban areas (e.g., electrical grid, public transportation) under significant stresses and/or failure (McEvoy, Ahmed, and Mullett, [2012](#); Zuo et al., [2015](#)). These events are projected to increase in frequency due to the effects of climate change. Projections indicate that the impacts of future climate will cause adverse effects of extreme heat to become more frequent and severe (Burillo et al., [2019](#); Forzieri et al., [2018](#); Peng et al., [2011](#)).

The meteorology of extreme heat events and its impacts on urban areas can be observed from the synoptic and local scales. From a synoptic scale, extreme heat events are often caused by the sustained presence of a high-pressure system over an area, resulting in lower wind speeds and warm air subsidence, promoting higher surface temperatures (Black et al., [2004](#); Miralles et al., [2014](#)). From a local perspective, the

amplified impact of extreme heat events on cities is a result of the urban heat island (UHI) effect, which occurs as a result of the modification of land surface properties due to the built environment. The modification of surface properties has been shown to increase near-surface air temperatures due to factors such as radiation entrapment, increased heat storage, and lower evapotranspirative cooling (Chen, Yang, and Zhu, 2014; Li and Elie Bou-Zeid, 2013; Ramamurthy and Bou-Zeid, 2017; Zhao et al., 2018). Additionally, urban areas near large bodies of water experience effects from the sea breeze, which has been shown to play a moderating influence on the intensity of the UHI effect (Hu and Xue, 2016; Jiang et al., 2019; Stéfanon et al., 2014). The processes on these two scales can be connected by understanding the structure and dynamics of the urban boundary layer (UBL), which is the lowest part of the troposphere in which surface-atmosphere exchanges occur that directly affect human activity. There have been a large number of numerical studies performed to improve our understanding of UBL processes during extreme heat events, which have been important for conceptualizing the role of synoptic-scale and surface forcings on urban climate. Something about the vertical structure of the UBL and coupling these

However, detailed observational analyses of UBL structure and dynamics are somewhat limited, especially in the vertical direction. Over the last 20 years, microwave radiometers, lidars, and radiosondes have been shown to be essential for accomplishing this. Microwave radiometers have been used to determine vertical profiles of temperature and water vapor (Rose et al., 2005; Z. Wang et al., 2012), while lidars being used to observe three-dimensional wind fields and aerosol concentrations (Grund et al., 2001). Although radiosondes provide direct measurements of the aforementioned properties in the boundary layer as it moves vertically through it, they present greater difficulties (e.g., cost, shorter supply) and are unable to observe at the temporal resolution of microwave radiometers and lidars.

Although somewhat limited in spatiotemporal scale, numerous observational campaigns have been performed to better our understanding of UBL structure and dynamics. Barlow et al. (2011) provides an in-depth study of boundary layer dynamics above London over a month-long period using a combination of a sonic anemometer and Doppler lidar, allowing for high-resolution vertical observations of a complex UBL and a better understanding of turbulent structures and vertical mixing processes. Similarly, Pelliccioni et al. (2012) employs a sonic anemometer and a sodar system at a site in Rome to observe and analyze the lower 200 m of the UBL to determine UBL characteristics and explore the validity of Monin-Obukhov similarity theory in the surface layer. Additionally, Arruda Moreira et al. (2020) evaluates the ability of lidar and microwave radiometer systems to observe turbulence over a variety of atmospheric conditions, including the effects of significant dust concentrations, in the region around Granada, Spain. Studies such as those performed by Banks et al. (2015), Quan et al. (2013), and Z. Wang et al. (2012) further demonstrate the ability of vertical profiling instruments to analyze the boundary layer structure by deriving UBL heights and its diurnal evolution. Expanding upon UBL structure, Anurose, Subrahmanyam, and Sunilkumar (2018) details a long-term observational campaign over an urban location in southern India that chronicles UBL height through monsoon season, annual averages of near-surface quantities, and the dynamics and effects of the sea breeze circulation.

Observations of the UBL during extreme heat events are even more limited. Ramamurthy and Bou-Zeid (2017) used microwave radiometers to observe the UBL over New York City in July 2016 to find that the UHI effect was amplified during heat wave events and that spatial variability throughout the city was significant throughout the observation period. Jiang et al. (2019) explores the effects of heat waves on rural and urban areas for several cities in China using ground-based observations with a focus on the UHI effect, finding that the effect was amplified during heat waves due to greater surface solar radiation and shifts in wind direction contributing to advection of heated air masses over the studied cities. (Wu et al., 2019) uses a combination of a ceilometer and multiple lidars to observe the evolution of UBL structure, air quality, and pollutant transport during a heat wave in New York City, demonstrating sharp rates of UBL growth due to convective activity and an increase of pollutant concentration and regional transport.

78 Zhang et al. (2020) uses aircraft-based observations to provide a comprehensive analysis of UBL structure
79 during heat wave events over cities in the United States throughout a 10-year period, providing insights
80 into the 'heat dome' thermodynamic structure over cities and the variability between heat wave events
81 due to local (such as surface properties in urban areas) and large-scale (such as synoptic meteorological
82 conditions) forcings.

83 New York City represents a complex case for urban meteorology given its diverse array of land cover
84 types (deciduous forest to supertall skyscrapers) and its proximity to multiple major bodies of water
85 (Lower New York Bay and the New York Bight to the south and east, Long Island Sound to the north
86 and east). Due to these factors, the effects of the surface energy budget (Hrisko, Prathap Ramamurthy,
87 and Gonzalez, 2021; Prathap Ramamurthy and Bou-Zeid, 2014; Tewari et al., 2019) and sea breezes
88 (Childs and Raman, 2005; Colle and Novak, 2010; Frizzola and Fisher, 1963; Gedzelman et al., 2003;
89 Melecio-Vázquez et al., 2018; Thompson, Holt, and Pullen, 2007) on the mesoscale meteorology have
90 been studied extensively. However, similar to studies of other urban areas mentioned previously, much
91 of this research has involved numerical simulations of these meteorological processes. In this study, we
92 attempt to further our understanding of the UBL over a coastal urban area by compiling observations
93 from multiple locations within New York City and analyzing the UBL using derived quantities.

94 This study attempts to use observations and analytical methods to provide insight into the following
95 questions:

- 96 1. How do UBL structure and dynamics depart from the climatology during extreme heat events?
- 97 2. How does the UBL structure impact the transport of scalars?
- 98 3. What effect does the sea breeze have on a coastal urban area during extreme heat events?

99 2 Data collection and analysis

100 2.1 Study site

101 The UBL over New York City is observed and analyzed in this study. Observational data was captured
102 at four locations within New York City (Table 1).

Table 1: Locations and details of observations sites.

	Bronx	Queens	Staten Island
Coordinates	40.87248°N, 73.89352°E	- 73.81585°E	- 74.14850°E
Elevation (m a.g.l.)	57.8	56.3	32.4
Element roughness height (m a.g.l.)			
Instruments used	Lidar, microwave radiometer	Lidar, microwave radiometer, sonic anemometer	Lidar, microwave radiometer, sonic anemometer
Valid wind directions	N/A	180 to 360°	None

104 2.2 Observational instruments

105 Observations of the UBL were made using a synthesis of microwave radiometers, lidars, and satellites.

106

107 Vertical profiles of temperature and vapor density were captured using a network of Radiometrics
108 MP-3000A microwave radiometers (Hewison and Gaffard, 2003) operated by the New York State
109 Mesonet (Brotzge et al., 2020). Profiles for water vapor are retrieved using 21 channels in the 22-30.0

110 GHz (K-band) range, while profiles for temperature are retrieved using 14 channels in the 51-59.0 GHz
111 (V-band) range. Profile accuracy (relative to radiosonde soundings) determined by performance studies
112 at various locations reported an annually-averaged water vapor accuracy within 1.0 g m^{-3} below 2 km
113 and an annually-averaged temperature accuracy within 1.6 K below 4 km (Güldner and Späckuch, 2001;
114 Sánchez et al., 2013). Quantities are captured at 58 height levels starting at ground level and ending
115 at 10 km above ground level, with vertical steps of 50 m from ground level to 500 m, 100 m from 500 m
116 to 2 km, and 250 m steps above 2 km. Observation integration times range from 0.01 to 2.50 s. Vertical
117 profiles are generated every 10 s and averaged over 10 min periods.

118
119 Wind measurements were measured using a network of Leosphere WindCube 100S Doppler lidars
120 operated by the New York State Mesonet (Brotzge et al., 2020). Measurements of wind motion using
121 the Doppler beam swinging scan mode in three directions: zonal (u), meridional (v), and vertical (w)
122 over 20 s cycles, with measurements averaged over 10 min intervals (Shrestha et al., 2021). The vertical
123 range of the WindCube 100S is 7 km above ground level with wind speed and direction accuracies of
124 0.5 m s^{-1} and 2° , respectively. The WindCube 100S has also been shown to perform with a high degree
125 of accuracy relative to radiosonde soundings, especially above 500 m (Kumer, Reuder, and Furevik, 2014).

126
127 Land and sea surface temperatures were estimated using derived products from the NOAA/NASA
128 GOES-16 Advanced Baseline Imager (ABI) (Ignatov et al., 2010; Yu et al., 2008). The GOES-16 ABI
129 provides a spatial resolution of 2 km with real-time data available to the public on an hourly basis.
130 The spatial extent of the Land Surface Temperature (LST) product ranges from the continental United
131 States (CONUS) to the majority of the Western Hemisphere (known as *full disk*), whereas the Sea
132 Surface Temperature (SST) product has a full disk spatial extent. The LST product has been found
133 to have an error relative to surface observations of 2.5 K over all land cover types, while sea surface
134 temperatures (SSTs) estimated using the GOES-16 ABI have been found to have an error relative to
135 shipborne radiometers $\leq 1 \text{ K}$ in the New York Bight (Luo and Minnett, 2021).

136 2.2.1 Data criteria & availability

137 Dates selected for this study are categorized into three groups: (1) normal days, (2) extreme heat days,
138 and (3) sea breeze days. For the purposes of this study, *extreme heat events* are defined as 3 or more
139 consecutive days with maximum daily temperatures exceeding 90°F (305 K), per the New York branch
140 of NOAA National Weather Service (Robinson, 2001; National Weather Service, 2018), while *normal*
141 *days* are defined as days that do not meet these criteria. Because the aim of this study is to observe the
142 effect of extreme heat on the UBL, normal day selection was restricted to months in which extreme heat
143 events occurred (May through September), as well as days in which 50% or more of the day featured
144 clear-sky conditions below 3.65 km above ground level due to the association of extreme heat events with
145 reduced daytime cloud coverage and precipitation (Stéfanon et al., 2014; Thomas et al., 2020). Clear-
146 sky conditions were identified by using an average of 5-minute surface-based observations from three
147 airports in the Automated Surface Observation System (ASOS) (NOAA et al., 1998) network within
148 the New York City metropolitan area: Newark Liberty International Airport (EWR), John F. Kennedy
149 International Airport, and LaGuardia Airport. *Sea breeze events* are identified as times during normal
150 and extreme heat days in which the low-level ($\leq 200 \text{ m}$) mean horizontal wind speed (U) is less than
151 5 m s^{-1} and low-level wind direction has a primarily easterly component, due to the presence of the
152 Atlantic Ocean to the east of New York City.

153 - Discuss quality filtering - Plots showing sampling counts per hour per site per day

154 **2.3 Derived quantities**

155 **3 Normal and extreme heat boundary layer properties**

156 This section discusses the differences in boundary layer structure and properties between normal days
157 and extreme heat events. Results are presented from the averages over all identified normal and heat
158 event days.

159 **3.1 Temperature**

160 On average, extreme heat events increase the temperature at the surface, as expected (see Figure
161 4). This is consistent across all observed locations in New York City, with the extreme heat event
162 temperature exceeding normal temperatures by approximately $1-\sigma$ over the entire day. An increase in
163 the difference is observed during daytime hours, with the difference peaking in magnitude around 13:00
164 LST at the hottest time of day. The surface temperature variability is significantly lower during heat
165 events ($\sigma = 1.77\text{ K}$) than during normal temperatures ($\sigma = 4.57\text{ K}$).
166

167 Above the surface, extreme heat events similarly increase the temperature significantly over the
168 lowest 3000 m of the troposphere (see Figure 3), with standardized anomalies of θ ranging from $\sigma = 0.88$
169 to 1.20. The largest temperature anomalies shift from the surface layer in the mornings to span the
170 entirety of the mixed layer. This is reflective of strong surface forcing resulting in convection through
171 the surface layer, as indicated by the formation of a late morning superadiabatic layer at all locations
172 (Figures 5, 6, 7).
173

174 The vertical profiles of θ suggests a degree of spatial variability exists between locations. One
175 instance of this spatial variability is vertical mixing; the Bronx site appears to have stronger vertical
176 mixing based on Figure 5, as θ remains constant for a greater height than at the Queens and Staten
177 Island locations. This phenomenon is more pronounced during extreme heat events, as a distinct mixed
178 layer is apparent in the Bronx during early (12:00 LST) and late (18:00 LST) afternoon hours. While
179 the mixed layer is also visible for the other locations, the strength of the mixed layer is emphasized by
180 the negative $\frac{d\theta}{dz}$ values between 1000 and 1500 m.
181

3.2 Moisture

182 On average, extreme heat events were found to increase the moisture at the surface, as indicated by
183 the diurnal profiles of specific humidity (q) (see Figure 9). This is also consistent across all observed
184 locations in New York City, with the extreme heat event temperature exceeding normal temperatures
185 by approximately $1-\sigma$ over the entire day. Although a distinct diurnal profiles exists (q decreases during
186 daytime hours), the diurnal range is smaller in magnitude than temperature. It is also worth noting
187 that the diurnal range is lower for Staten Island than for the Bronx or Queens, suggesting that degree of
188 urbanization has a negative correlation with the diurnal range of q . Similar to surface temperature, the
189 variability of q is significantly lower during heat events ($\sigma = 2.14 \times 10^{-3} \text{ kg kg}^{-1}$) than during normal
190 temperatures ($\sigma = 3.18 \times 10^{-3} \text{ kg kg}^{-1}$).
191

192 In the boundary layer, the positive q anomalies subside in magnitude between 300 and 600 m,
193 but increase significantly in the mixed layer, especially during the late morning and early afternoon
194 for all sites. As shown in Figure 8, the largest anomalies occur between 10:00 and 16:00 LST in the
195 upper mixed layer. With regards to spatial variation in q , the highest anomalies occur over the Bronx
196 and Queens, whereas Staten Island demonstrates a positive q anomaly with lower magnitudes during
197 extreme heat events. This correlates with the magnitude of the difference in surface quantities shown in
198 Figure 9.
199

199

200 With regards to time, mid-morning increases in anomaly values in the lower mixed layer (~ 500 m)
 201 suggest enhanced vertical transport of moisture across all sites (see Figures 10, 11, 12). Vertical profiles
 202 of q across all locations show markedly higher q values at the surface during extreme heat event with $\frac{dq}{dz}$
 203 values increasing throughout the morning in the mixed layer while low-level q values decrease, indicating
 204 vertical transport of moisture and drier low-level conditions during peak insolation.

205 3.3 UBL dynamics

206 3.3.1 Horizontal winds

207 Extreme heat events resulted in an overall reduction of horizontal wind speeds (U) in the UBL. More
 208 specifically, the magnitude of U during extreme heat events is similar in magnitude to U during normal
 209 days with the exception of early morning hours and at upper levels of the UBL. As shown in Figure
 210 13, modest reductions in U ($-1.2 \leq \sigma \leq -0.4$) during extreme heat events are present throughout the
 211 UBL from early to mid-morning, with little differences throughout the rest of the day ($-0.4 \leq \sigma \leq 0.4$).
 212 Larger deviations between U values are present at the top of the UBL where synoptic conditions become
 213 dominant.

214

215 Vertical profiles of U for normal and extreme heat events provide a more detailed view of the
 216 differences in UBL structure. Across all sites, U is similar throughout the UBL overnight, afternoon,
 217 and evenings. During early morning hours, extreme heat event U values decrease by 25 to 50%
 218 throughout the entire UBL (see Figures 15, 16, 17), although both event types present a classical
 219 logarithmic wind profile, with surface friction effects present through 500 m. Another phenomenon
 220 worth noting is the difference in U profiles above 2000 m; profiles of U during extreme heat events
 221 are more consistent between sites and vertically than during normal days. This phenomenon may
 222 highlight the effect of synoptic meteorological conditions on U , as the UBL typically remains below
 223 2500 m. During extreme heat events, anticyclonic conditions produce more stable atmospheric con-
 224 ditions relative to normal days, resulting in less variability between heat events than during normal days.
 225

226 Extreme heat events result in a southwesterly shift in U throughout the UBL. This shift is present most
 227 evidently closer to the surface, as shown in Figures 18, 19, and 20, with winds at 100 m coming primarily
 228 from the southwest quadrant. Figure 19 shows that Queens also presents a secondary maximum with
 229 winds approaching from the south, which suggests effects from the Atlantic sea breeze (effects from
 230 the sea breeze will be further discussed in Section 4). At 1000 m, the directionality of prevailing winds
 231 becomes more uniform between normal and extreme heat days, as winds primarily approach New
 232 York City from the west-southwest. The disparity in wind directions between 100 and 1000 m suggests
 233 that localized wind fields play a major role in UBL dynamics at lower levels whereas synoptic-scale
 234 atmospheric conditions increasingly dominate with increasing height.

235

236

237 3.3.2 Vertical motion

238 On average, extreme heat events do not appear to produce significant changes in vertical velocity (w).
 239 Figure 24 shows average diurnal profiles of w at all locations at 100 m above ground level, with similar
 240 mean values throughout the day between normal days and extreme heat events. During extreme heat
 241 events, however, the variability of w is less in the early morning hours and greater in the evening. This
 242 phenomenon is also observed in vertical profiles of w at all locations as shown in Figures 26, 27, and
 243 28. At all locations, overnight and morning profiles of w (0:00 and 6:00 LST) show significantly lower
 244 variability in w throughout the UBL with similar magnitudes of mean w . Despite similar means and

245 deviations in the early afternoon (12:00 LST), evening profiles (18:00 LST) show significantly higher
246 variability in w below 500 m for all sites, with the Bronx showing this occurrence extend through the
247 UBL.

248 4 Effects of the sea breeze circulation

249 - Talk about sea breeze event frequency - Talk about synoptic conditions that are characteristic of sea
250 breeze events in New York

251 During extreme heat events, observations show that the sea breeze plays a moderating role on surface
252 conditions by reducing low-level temperatures and increasing low-level moisture content, as shown in
253 Figures 29 and 30.

254 Sea breezes in New York City occur as a result of land-sea temperature gradients from two arms of the
255 Atlantic Ocean; the New York Bight to the southeast and Long Island Sound to the northeast.

256 During days with identified sea breeze circulations, southeasterly winds increased in occurrence frequency
257 compared to all other days at all locations, especially after 12:00 LST. The occurrence frequency of
258 southeasterly winds is correlated with the distance between the observation site and the largest body
259 of water in proximity of the metropolitan area (Atlantic Ocean), as Staten Island reported 92.1% of
260 all winds at 100 m as southeasterly between 12:00 and 20:00 LST (distance of 6.50 km from Lower New
261 York Bay), whereas Queens reported 67.4% (distance of 16.5 km), and Bronx reported 55.6% (distance
262 of 32.9 km).

263 5 Discussion

264 6 Conclusions

265 Acknowledgments

266 This research is made possible by the New York State (NYS) Mesonet. Original funding for the NYS
267 Mesonet was provided by Federal Emergency Management Agency grant FEMA-4085-DR-NY, with the
268 continued support of the NYS Division of Homeland Security & Emergency Services; the state of New
269 York; the Research Foundation for the State University of New York (SUNY); the University at Albany,
270 SUNY; the Atmospheric Sciences Research Center (ASRC) at SUNY Albany; and the Department of
271 Atmospheric and Environmental Sciences (DAES) at SUNY Albany.

272 References

- 273 Anderson, G Brooke and Michelle L Bell (2011). "Heat waves in the United States: mortality risk during heat
274 waves and effect modification by heat wave characteristics in 43 US communities". In: *Environmental health
275 perspectives* 119.2, pp. 210–218.
- 276 Anurose, TJ, D Bala Subrahmanyam, and SV Sunilkumar (2018). "Two years observations on the diurnal
277 evolution of coastal atmospheric boundary layer features over Thiruvananthapuram (8.5° N, 76.9° E), India".
278 In: *Theoretical and applied climatology* 131.1, pp. 77–90.
- 279 Arruda Moreira, Gregori de et al. (2020). "Study of the planetary boundary layer height in an urban environment
280 using a combination of microwave radiometer and ceilometer". In: *Atmospheric Research* 240, p. 104932.
- 281 Banks, Robert F et al. (2015). "Performance evaluation of the boundary-layer height from lidar and the Weather
282 Research and Forecasting model at an urban coastal site in the north-east Iberian Peninsula". In: *Boundary-
283 layer meteorology* 157.2, pp. 265–292.
- 284 Barlow, Janet F et al. (2011). "Boundary layer dynamics over London, UK, as observed using Doppler lidar
285 during REPARTEE-II". In: *Atmospheric Chemistry and Physics* 11.5, pp. 2111–2125.

- 286 Black, Emily et al. (2004). "Factors contributing to the summer 2003 European heatwave". In: *Weather* 59.8,
287 pp. 217–223.
- 288 Brotzge, Jerald A et al. (2020). "A technical overview of the new york state mesonet standard network". In:
289 *Journal of Atmospheric and Oceanic Technology* 37.10, pp. 1827–1845.
- 290 Burillo, Daniel et al. (2019). "Electricity infrastructure vulnerabilities due to long-term growth and extreme heat
291 from climate change in Los Angeles County". In: *Energy Policy* 128, pp. 943–953.
- 292 Chen, Feng, Xuchao Yang, and Weiping Zhu (2014). "WRF simulations of urban heat island under hot-weather
293 synoptic conditions: The case study of Hangzhou City, China". In: *Atmospheric research* 138, pp. 364–377.
- 294 Childs, Peter P and Sethu Raman (2005). "Observations and numerical simulations of urban heat island and sea
295 breeze circulations over New York City". In: *Pure and Applied Geophysics* 162.10, pp. 1955–1980.
- 296 Colle, Brian A and David R Novak (2010). "The New York Bight jet: climatology and dynamical evolution". In:
297 *Monthly Weather Review* 138.6, pp. 2385–2404.
- 298 Forzieri, Giovanni et al. (2018). "Escalating impacts of climate extremes on critical infrastructures in Europe".
299 In: *Global environmental change* 48, pp. 97–107.
- 300 Frizzola, John A and Edwin L Fisher (1963). "A series of sea breeze observations in the New York City area".
301 In: *Journal of Applied Meteorology and Climatology* 2.6, pp. 722–739.
- 302 Frumkin, Howard (2016). "Urban sprawl and public health". In: *Public health reports*.
- 303 Gedzelman, SD et al. (2003). "Mesoscale aspects of the urban heat island around New York City". In: *Theoretical
304 and applied climatology* 75.1, pp. 29–42.
- 305 Grund, Christian J et al. (2001). "High-resolution Doppler lidar for boundary layer and cloud research". In:
306 *Journal of Atmospheric and Oceanic Technology* 18.3, pp. 376–393.
- 307 Güldner, J and D Spänkuch (2001). "Remote sensing of the thermodynamic state of the atmospheric boundary
308 layer by ground-based microwave radiometry". In: *Journal of Atmospheric and Oceanic Technology* 18.6,
309 pp. 925–933.
- 310 Heaviside, Clare, Helen Macintyre, and Sotiris Vardoulakis (2017). "The urban heat island: implications for health
311 in a changing environment". In: *Current environmental health reports* 4.3, pp. 296–305.
- 312 Hewison, Tim and Catherine Gaffard (2003). "Radiometrics MP3000 microwave radiometer performance assess-
313 ment". In: *Obs. Development Technical Report TR29, Met Office, National Meteorological Library, Exeter,
314 UK. Also available from <http://tim.hewison.org/TR29.pdf>*.
- 315 Hrisko, Joshua, Prathap Ramamurthy, and Jorge E Gonzalez (2021). "Estimating heat storage in urban areas
316 using multispectral satellite data and machine learning". In: *Remote Sensing of Environment* 252, p. 112125.
- 317 Hu, Xiao-Ming and Ming Xue (2016). "Influence of synoptic sea-breeze fronts on the urban heat island intensity
318 in Dallas–Fort Worth, Texas". In: *Monthly Weather Review* 144.4, pp. 1487–1507.
- 319 Ignatov, A et al. (2010). "GOES-R Advanced Baseline Imager (ABI) algorithm theoretical basis document for
320 sea surface temperature". In: *NOAA NESDIS Center for Satellite Applications and Research*.
- 321 Jiang, Shaojing et al. (2019). "Amplified urban heat islands during heat wave periods". In: *Journal of Geophysical
322 Research: Atmospheres* 124.14, pp. 7797–7812.
- 323 Kumer, Valerie-M, Joachim Reuder, and Birgitte R Furevik (2014). "A comparison of LiDAR and radiosonde
324 wind measurements". In: *Energy Procedia* 53, pp. 214–220.
- 325 Li, Dan and Elie Bou-Zeid (2013). "Synergistic interactions between urban heat islands and heat waves: The
326 impact in cities is larger than the sum of its parts". In: *Journal of Applied Meteorology and Climatology* 52.9,
327 pp. 2051–2064.
- 328 Luo, Bingkun and Peter J Minnett (2021). "Skin Sea Surface Temperatures From the GOES-16 ABI Validated
329 With Those of the Shipborne M-AERI". In: *IEEE Transactions on Geoscience and Remote Sensing* 59.12,
330 pp. 9902–9913.
- 331 Madrigano, Jaime et al. (2015). "A case-only study of vulnerability to heat wave-related mortality in New York
332 City (2000–2011)". In: *Environmental health perspectives* 123.7, pp. 672–678.
- 333 McEvoy, Darryn, Iftekhar Ahmed, and Jane Mullett (2012). "The impact of the 2009 heat wave on Melbourne's
334 critical infrastructure". In: *Local Environment* 17.8, pp. 783–796.
- 335 Melecio-Vázquez, David et al. (2018). "Thermal Structure of a Coastal–Urban Boundary Layer". In: *Boundary-
336 Layer Meteorology* 169 (1), pp. 151–161. ISSN: 15731472. DOI: [10.1007/s10546-018-0361-7](https://doi.org/10.1007/s10546-018-0361-7). URL: <https://doi.org/10.1007/s10546-018-0361-7>.
- 338 Miralles, Diego G et al. (2014). "Mega-heatwave temperatures due to combined soil desiccation and atmospheric
339 heat accumulation". In: *Nature geoscience* 7.5, pp. 345–349.

- 340 National Weather Service, NOAA (May 2018). *National Weather Service New York, NY excessive heat page*. URL:
 341 <https://www.weather.gov/okx/excessiveheat>.
- 342 NOAA et al. (1998). *Automated Surface Observing System (ASOS) User's Guide*. URL: <https://www.weather.gov/media/asos/aum-toc.pdf>.
- 343 Pelliccioni, A et al. (2012). "Some characteristics of the urban boundary layer above Rome, Italy, and applicability
 344 of Monin–Obukhov similarity". In: *Environmental fluid mechanics* 12.5, pp. 405–428.
- 345 Peng, Roger D et al. (2011). "Toward a quantitative estimate of future heat wave mortality under global climate
 346 change". In: *Environmental health perspectives* 119.5, pp. 701–706.
- 347 Quan, Jiannong et al. (2013). "Evolution of planetary boundary layer under different weather conditions, and its
 348 impact on aerosol concentrations". In: *Particuology* 11.1, pp. 34–40.
- 349 Ramamurthy, P and E Bou-Zeid (2017). "Heatwaves and urban heat islands: a comparative analysis of multiple
 350 cities". In: *Journal of Geophysical Research: Atmospheres* 122.1, pp. 168–178.
- 351 Ramamurthy, Prathap and E Bou-Zeid (2014). "Contribution of impervious surfaces to urban evaporation". In:
 352 *Water Resources Research* 50.4, pp. 2889–2902.
- 353 Robinson, Peter J (2001). "On the definition of a heat wave". In: *Journal of Applied Meteorology and Climatology*
 354 40.4, pp. 762–775.
- 355 Rose, Thomas et al. (2005). "A network suitable microwave radiometer for operational monitoring of the cloudy
 356 atmosphere". In: *Atmospheric research* 75.3, pp. 183–200.
- 357 Sánchez, JL et al. (2013). "A method to improve the accuracy of continuous measuring of vertical profiles of
 358 temperature and water vapor density by means of a ground-based microwave radiometer". In: *Atmospheric
 359 Research* 122, pp. 43–54.
- 360 Shrestha, Bhupal et al. (2021). "Overview and Applications of the New York State Mesonet Profiler Network".
 361 In: *Journal of Applied Meteorology and Climatology* 60.11, pp. 1591–1611.
- 362 Stéfanon, Marc et al. (2014). "Soil moisture-temperature feedbacks at meso-scale during summer heat waves over
 363 Western Europe". In: *Climate dynamics* 42.5, pp. 1309–1324.
- 364 Tewari, Mukul et al. (2019). "Interaction of urban heat islands and heat waves under current and future climate
 365 conditions and their mitigation using green and cool roofs in New York City and Phoenix, Arizona". In:
 366 *Environmental Research Letters* 14.3, p. 034002.
- 367 Thomas, Natalie P et al. (2020). "Mechanisms associated with daytime and nighttime heat waves over the
 368 contiguous united states". In: *Journal of Applied Meteorology and Climatology* 59.11, pp. 1865–1882.
- 369 Thompson, William T, Teddy Holt, and Julie Pullen (2007). "Investigation of a sea breeze front in an urban envi-
 370 ronment". In: *Quarterly Journal of the Royal Meteorological Society: A journal of the atmospheric sciences,
 371 applied meteorology and physical oceanography* 133.624, pp. 579–594.
- 372 Wang, Z et al. (2012). "Lidar measurement of planetary boundary layer height and comparison with microwave
 373 profiling radiometer observation". In: *Atmospheric Measurement Techniques* 5.8, pp. 1965–1972.
- 374 Wu, Yonghua et al. (2019). "Observation of heat wave effects on the urban air quality and PBL in New York
 375 City area". In: *Atmospheric Environment* 218, p. 117024.
- 376 Yu, Yunyue et al. (2008). "Developing algorithm for operational GOES-R land surface temperature product". In:
 377 *IEEE Transactions on Geoscience and Remote Sensing* 47.3, pp. 936–951.
- 378 Zhang, Yuanjie et al. (2020). "Aircraft observed diurnal variations of the planetary boundary layer under heat
 379 waves". In: *Atmospheric Research* 235, p. 104801.
- 380 Zhao, Lei et al. (2018). "Interactions between urban heat islands and heat waves". In: *Environmental research
 381 letters* 13.3, p. 034003.
- 382 Zuo, Jian et al. (2015). "Impacts of heat waves and corresponding measures: a review". In: *Journal of Cleaner
 383 Production* 92, pp. 1–12.

385 **Appendix**

Table 2: Symbols and abbreviations used in the paper.

386

Symbol/Abbreviation	Definition
σ	Standard deviation
θ	Potential temperature
q	Specific humidity
U	Horizontal wind speed
w	Vertical velocity
UBL	Urban boundary layer
MLH	Mixed layer height

387 **Figures**

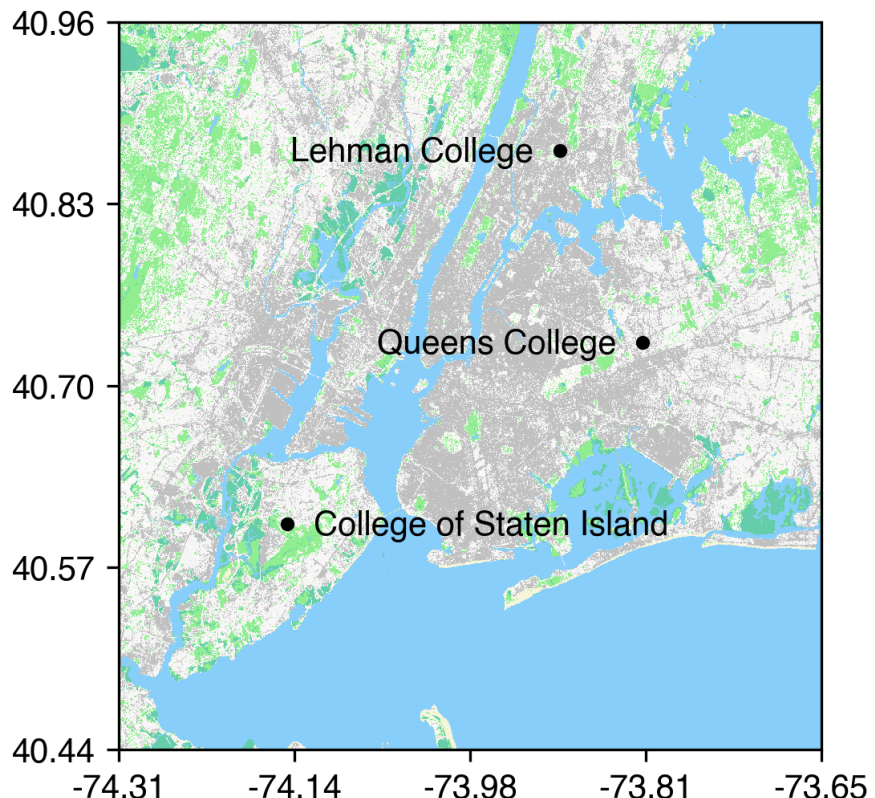


Figure 1: Observation sites overlaid on NLCD land cover types..

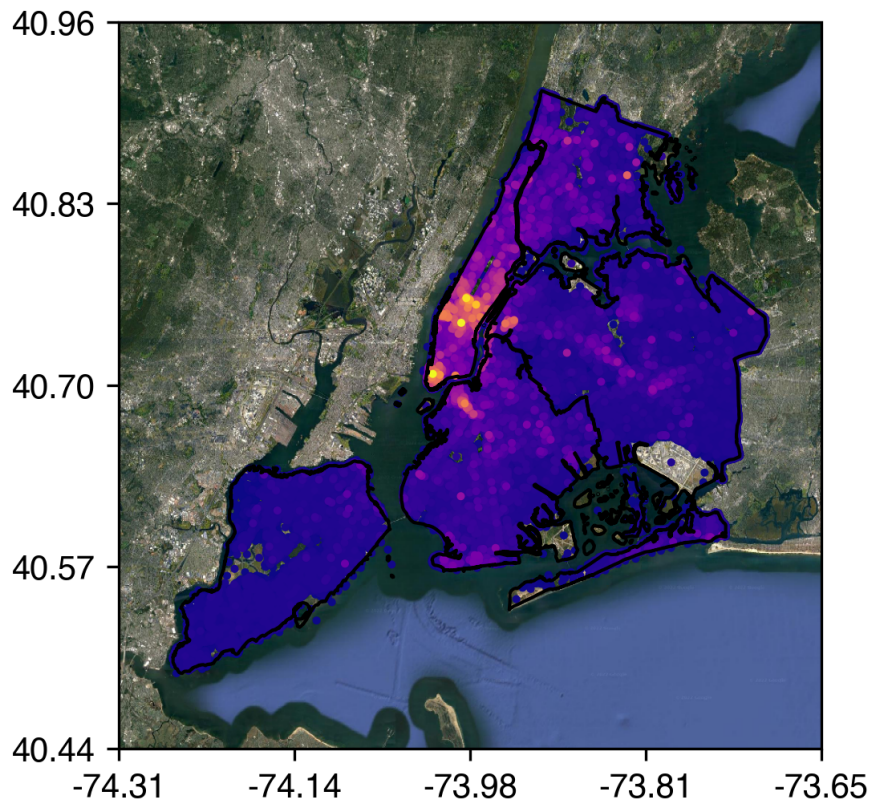


Figure 2: Building heights in New York City. Taken from NYC DOB data.

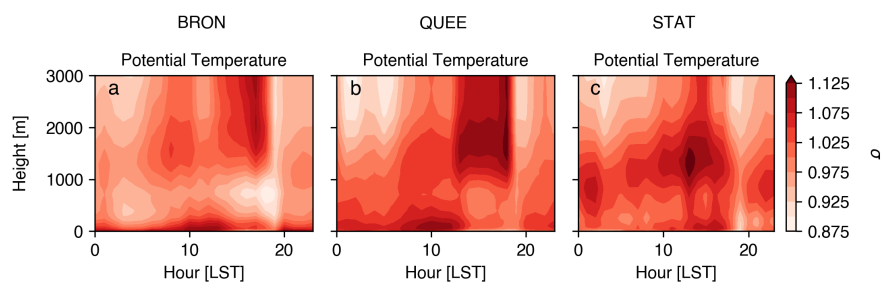


Figure 3: Anomalies of θ during extreme heat events relative to the climatology over the urban boundary layer.

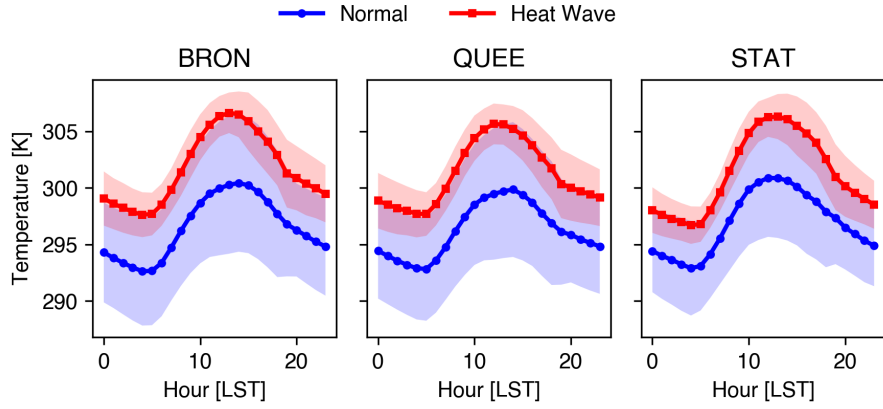


Figure 4: Anomalies of temperature during extreme heat events relative to the climatology at the surface.

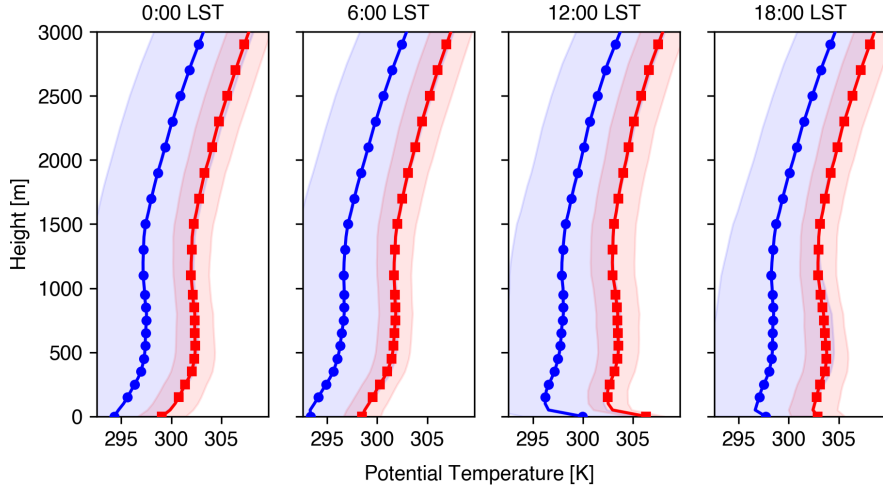


Figure 5: Vertical profiles of θ in the Bronx during normal days (blue) and extreme heat events (red).

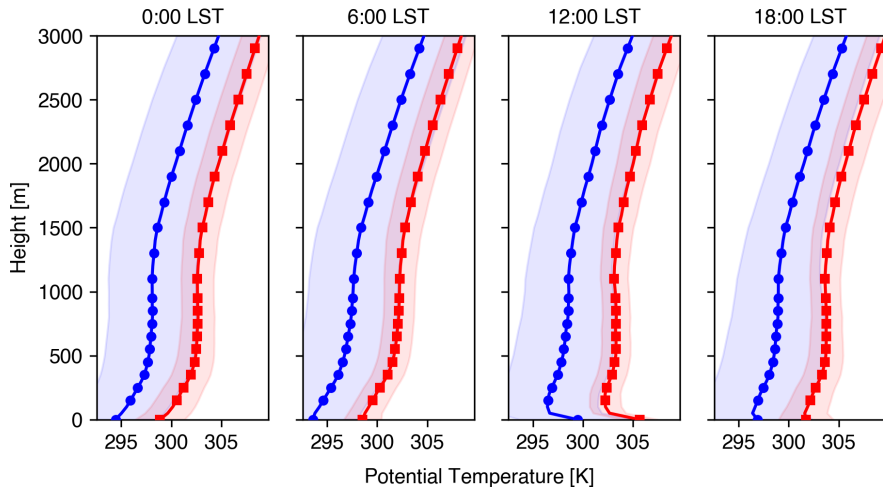


Figure 6: Vertical profiles of θ in Queens during normal days (blue) and extreme heat events (red).

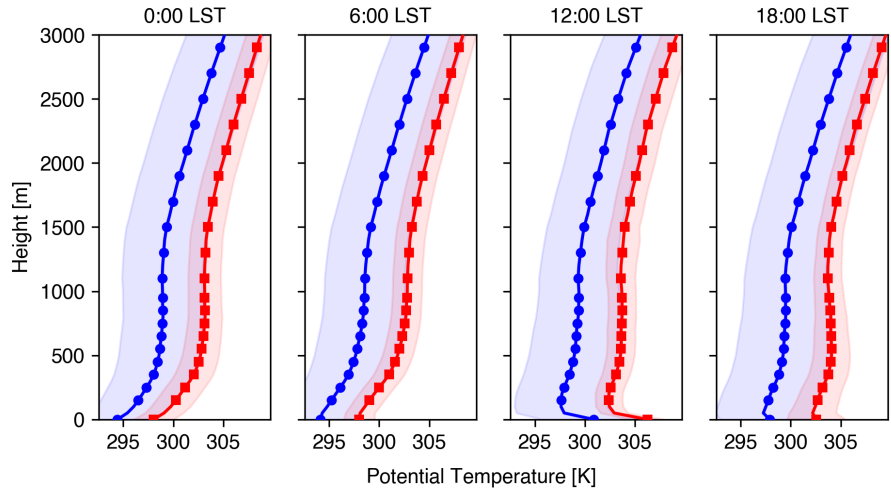


Figure 7: Vertical profiles of θ in Staten Island during normal days (blue) and extreme heat events (red).

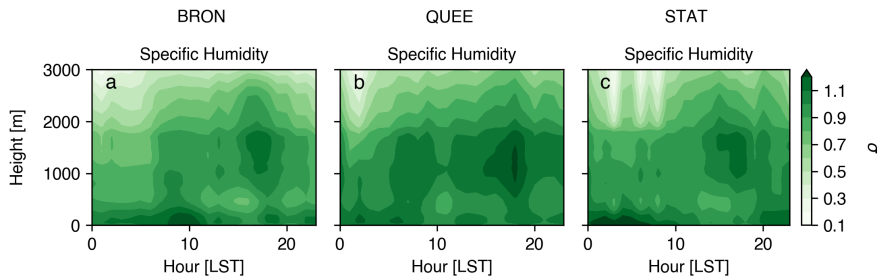


Figure 8: Anomalies of q during extreme heat events relative to the climatology over the urban boundary layer.

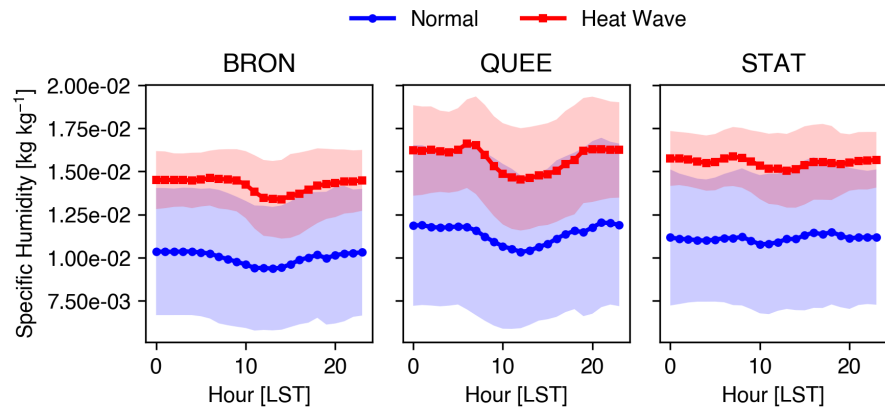


Figure 9: Anomalies of q during extreme heat events relative to the climatology at the surface.

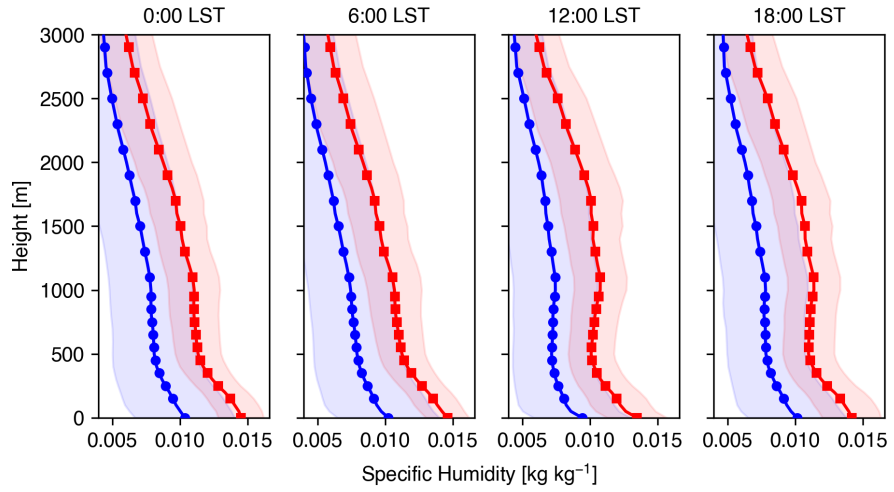


Figure 10: Vertical profiles of q in the Bronx during normal days (blue) and extreme heat events (red).

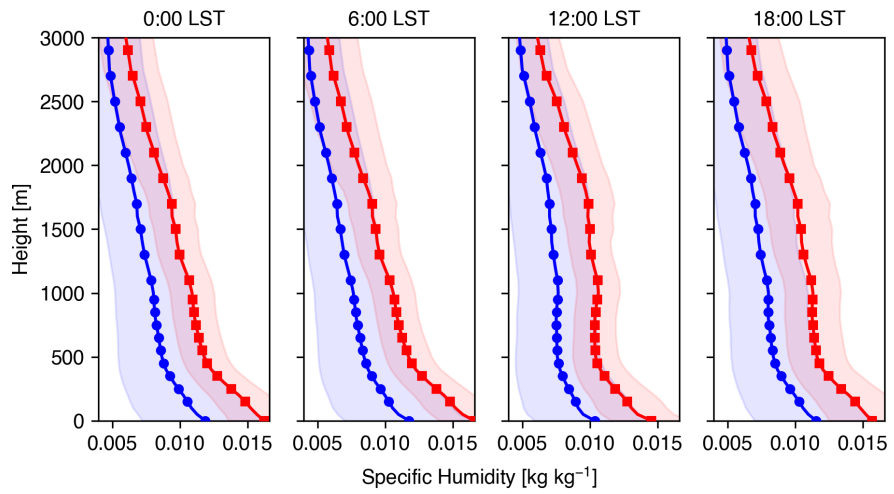


Figure 11: Vertical profiles of q in Queens during normal days (blue) and extreme heat events (red).

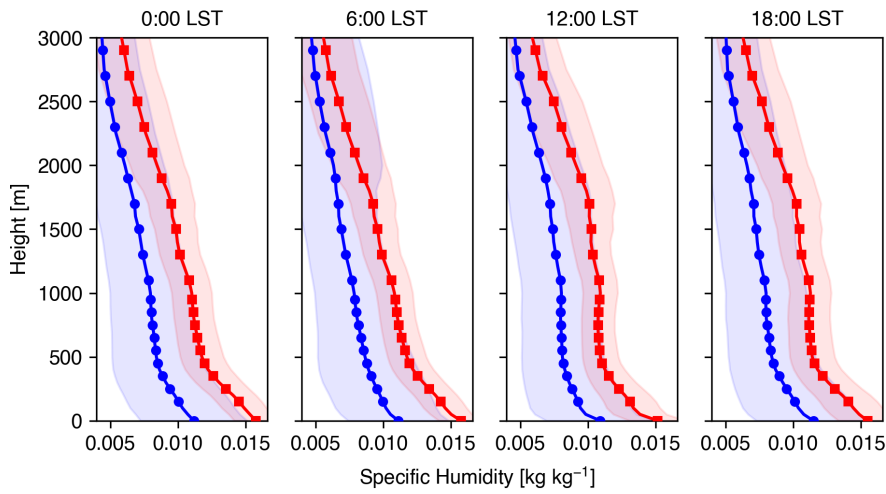


Figure 12: Vertical profiles of q in Staten Island during normal days (blue) and extreme heat events (red).

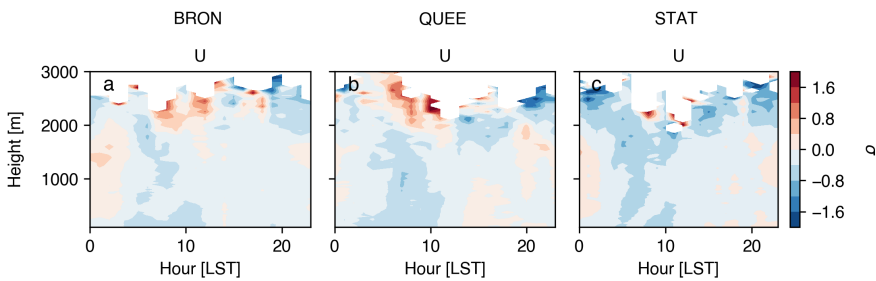


Figure 13: Anomalies of U during extreme heat events relative to the climatology over the urban boundary layer.

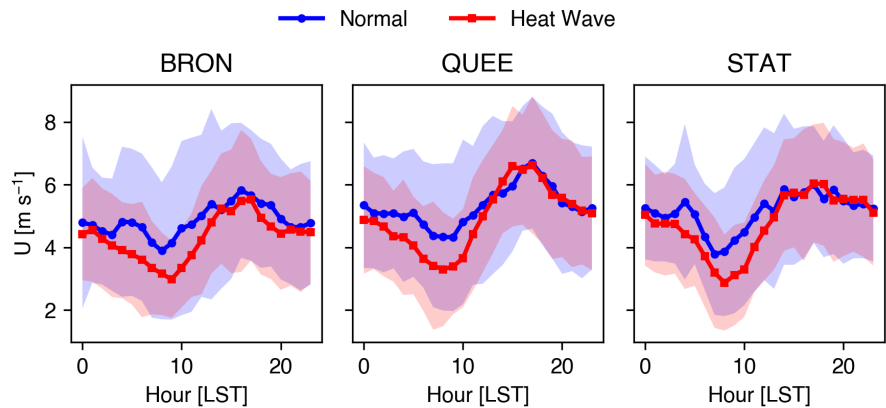


Figure 14: Anomalies of low-level U during extreme heat events relative to the climatology.

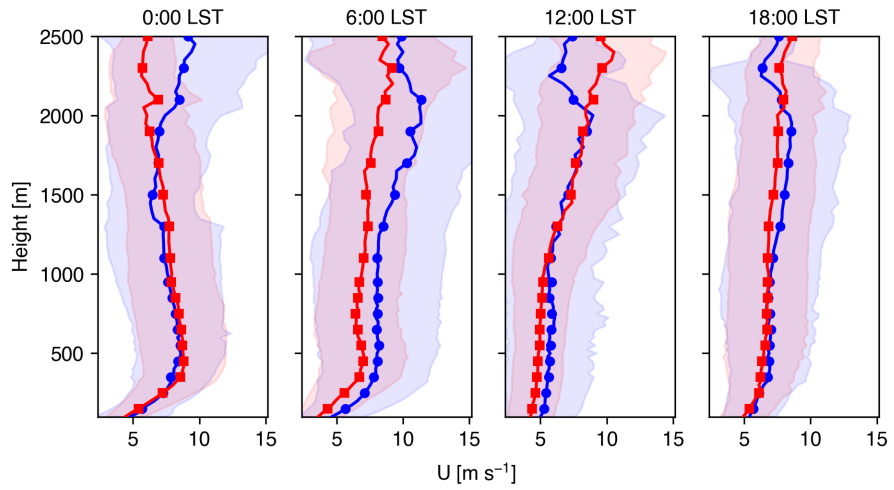


Figure 15: Vertical profiles of U in the Bronx during normal days (blue) and extreme heat events (red).

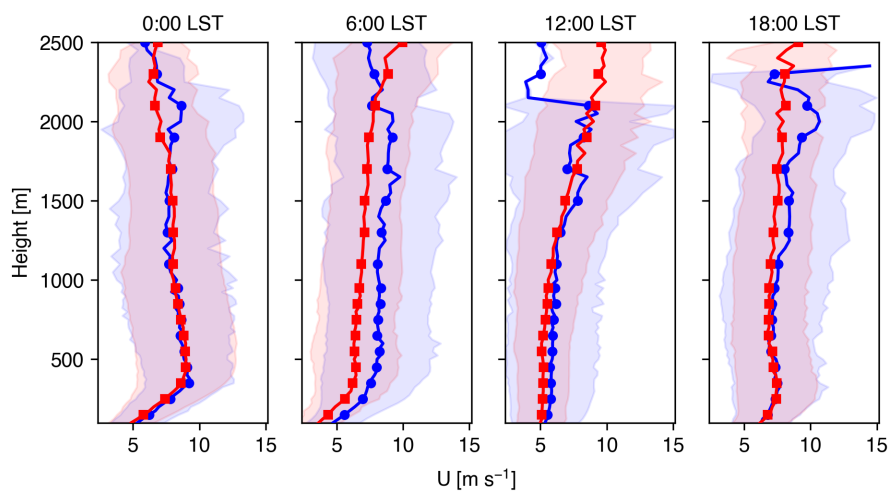


Figure 16: Vertical profiles of U in Queens during normal days (blue) and extreme heat events (red).

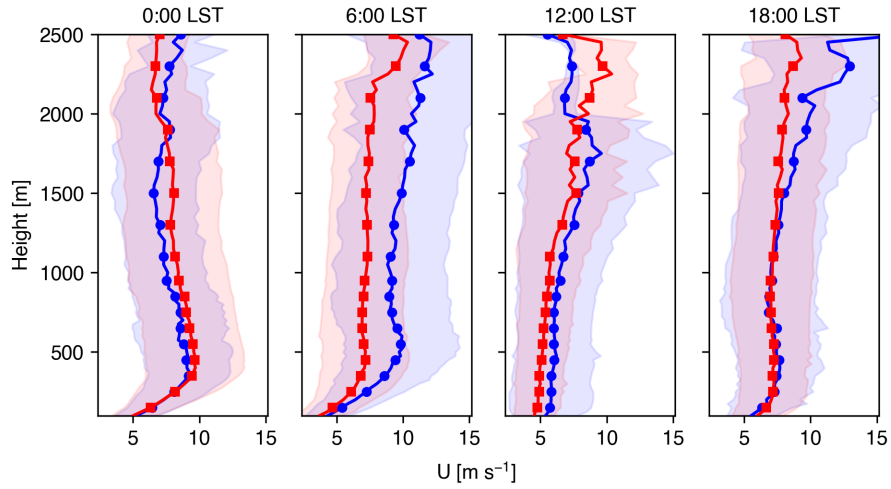


Figure 17: Vertical profiles of U in Staten Island during normal days (blue) and extreme heat events (red).

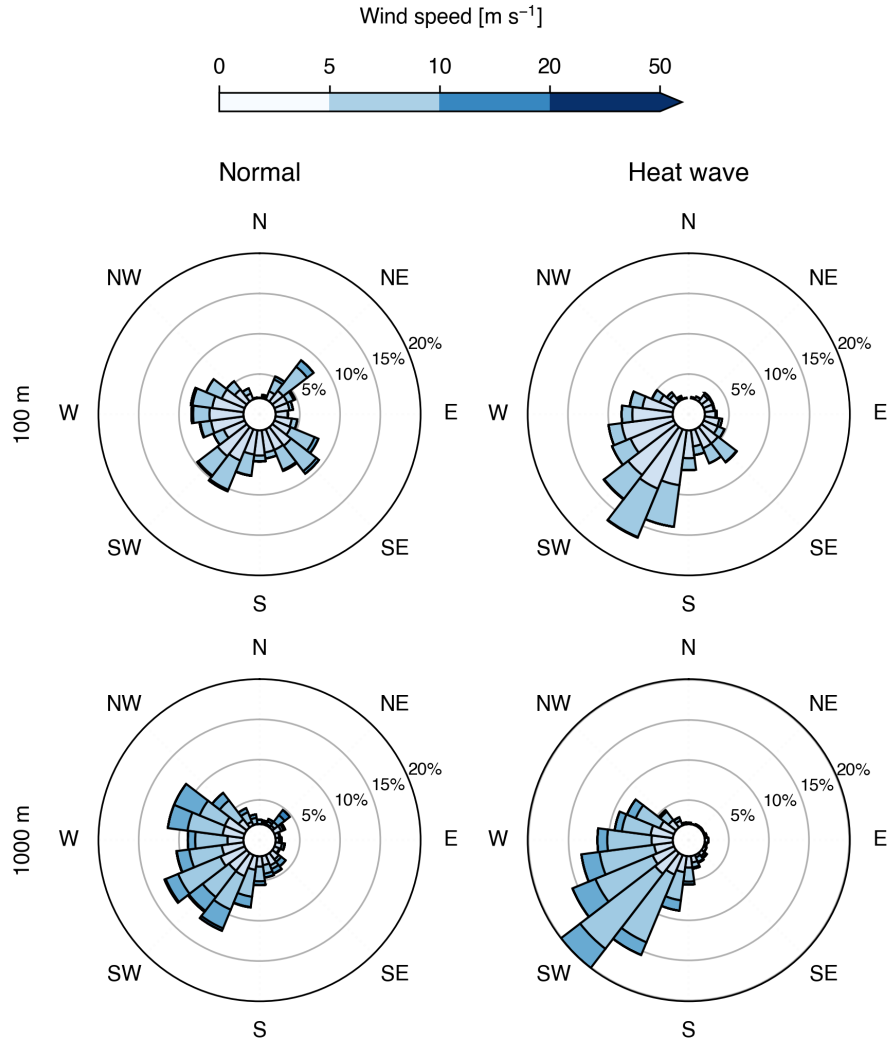


Figure 18: Horizontal winds in the lower-level (100 m) and mid-level of the urban boundary layer over the Bronx.

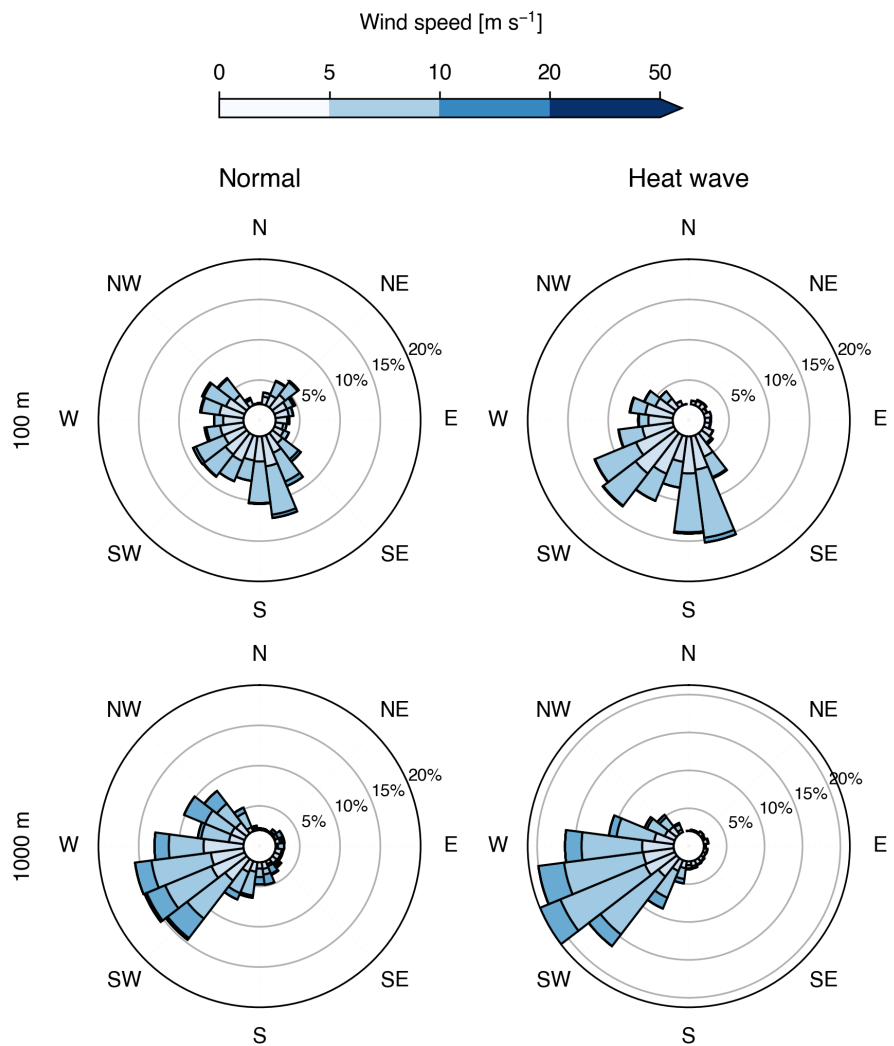


Figure 19: Horizontal winds in the lower-level (100 m) and mid-level of the urban boundary layer over Queens.

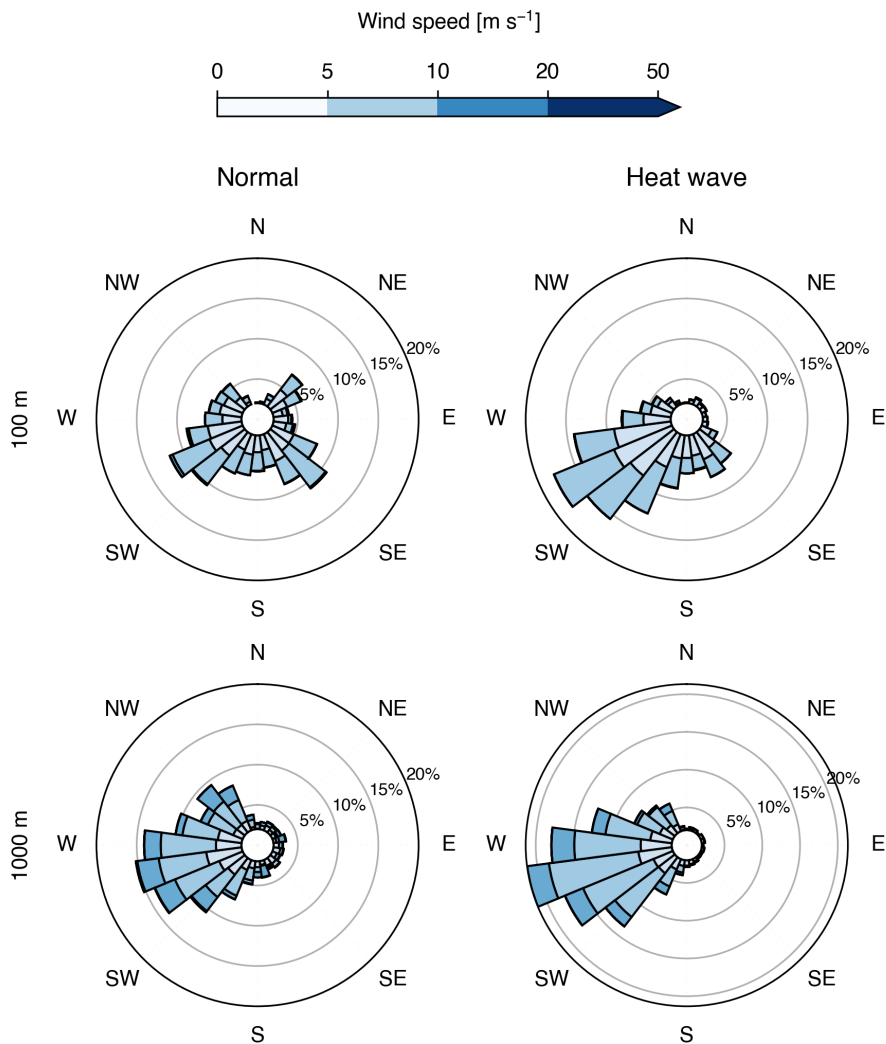


Figure 20: Horizontal winds in the lower-level (100 m) and mid-level of the urban boundary layer over Staten Island.

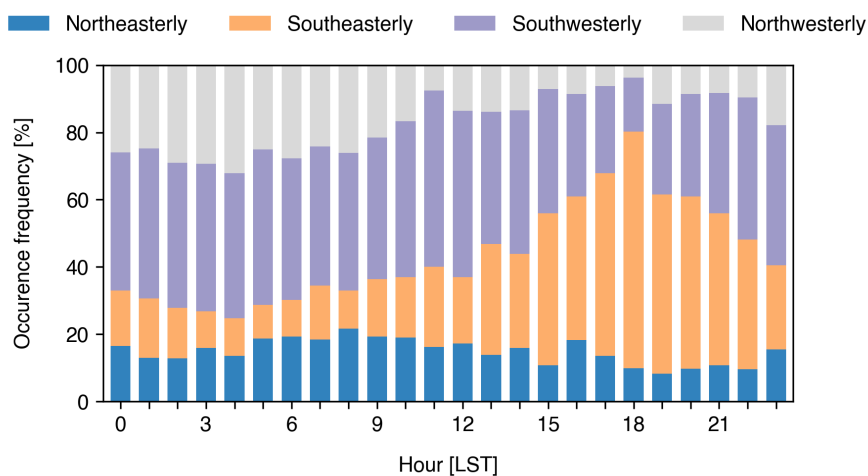


Figure 21: Diurnal evolution of low-level wind directions in the Bronx during normal days.

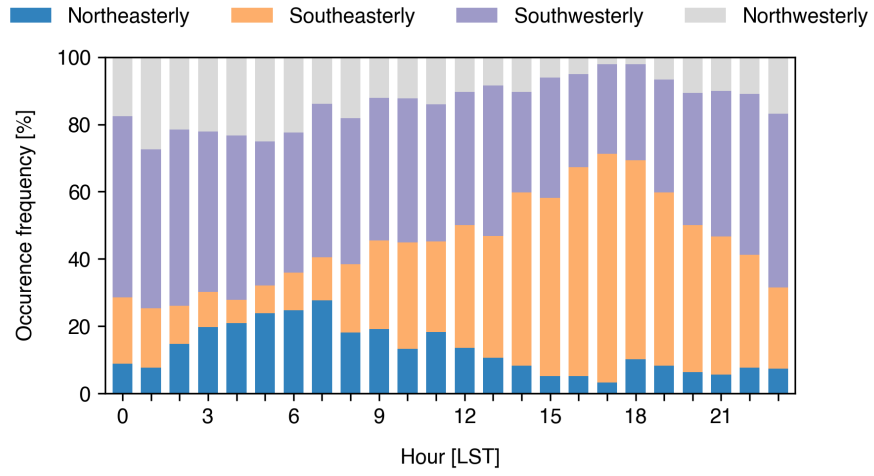


Figure 22: Diurnal evolution of low-level wind directions in Queens during normal days.

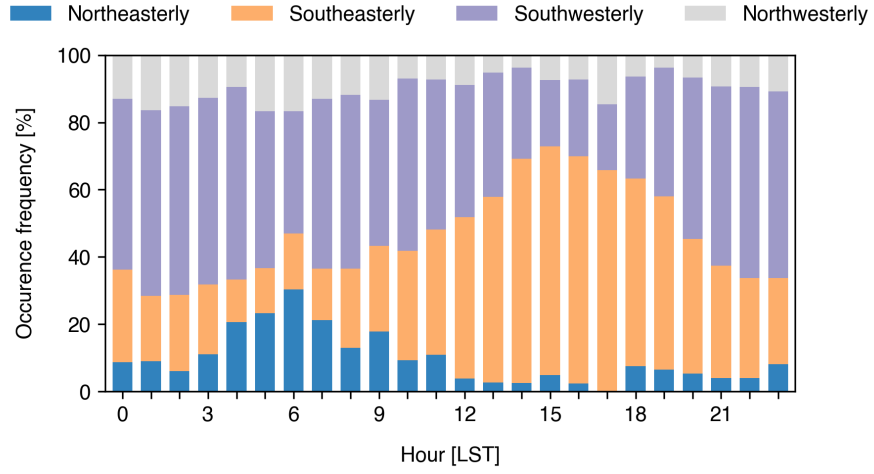


Figure 23: Diurnal evolution of low-level wind directions in Staten Island during normal days.

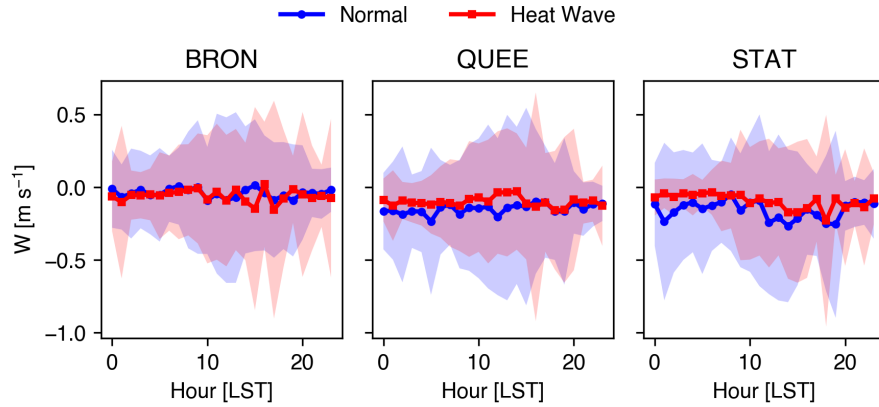


Figure 24: Anomalies of low-level w during extreme heat events relative to the climatology.

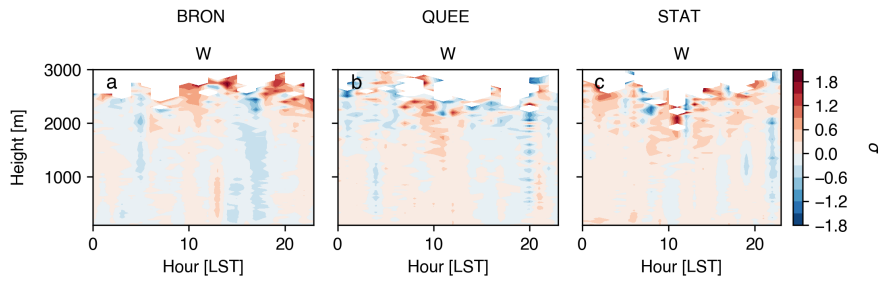


Figure 25: Anomalies of w during extreme heat events relative to the climatology over the urban boundary layer.

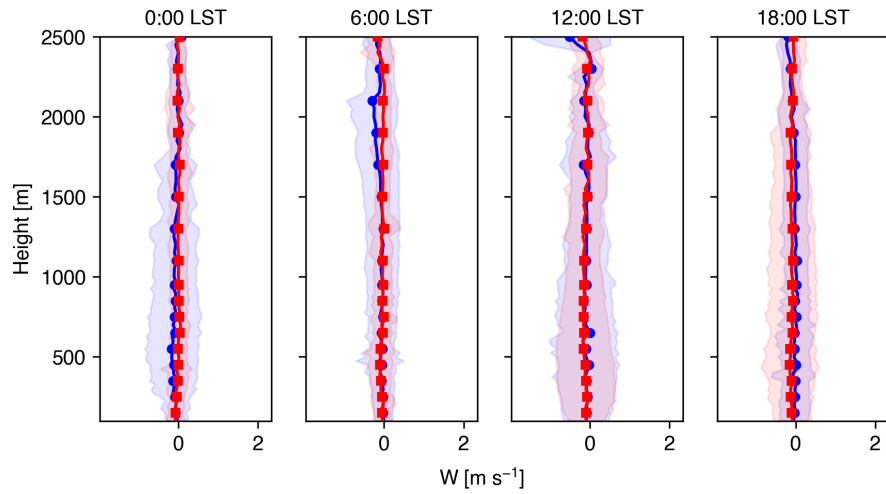


Figure 26: Vertical profiles of w in the Bronx during normal days (blue) and extreme heat events (red).

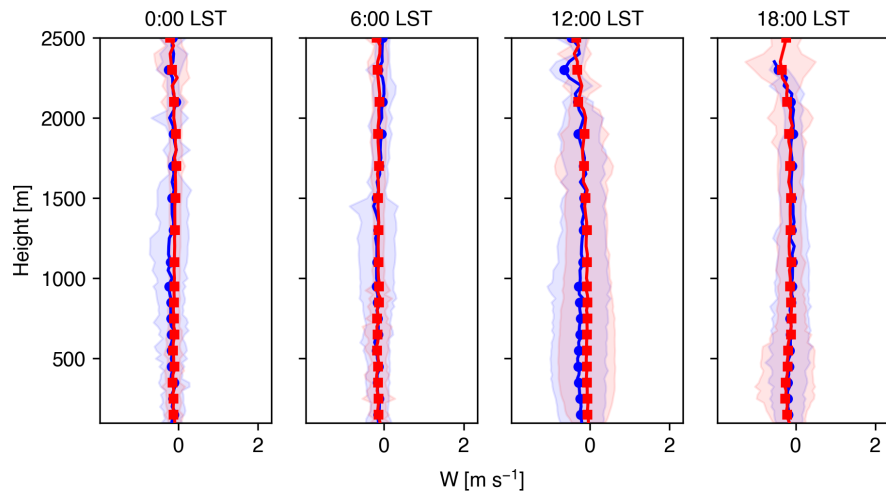


Figure 27: Vertical profiles of w in Queens during normal days (blue) and extreme heat events (red).

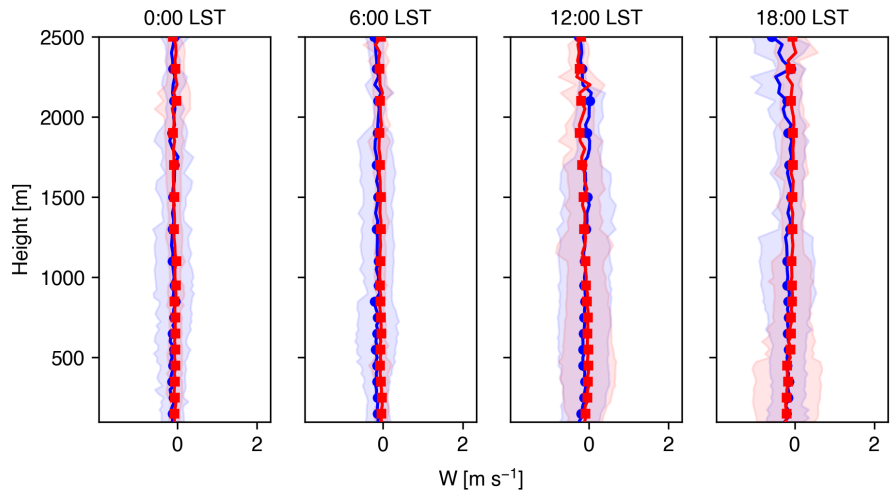


Figure 28: Vertical profiles of U in Staten Island during normal days (blue) and extreme heat events (red).

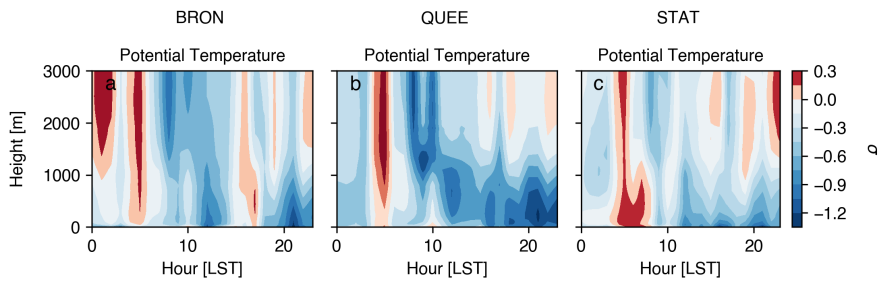


Figure 29: Anomalies of θ for heat wave days with a sea breeze relative to heat wave days without a sea breeze.

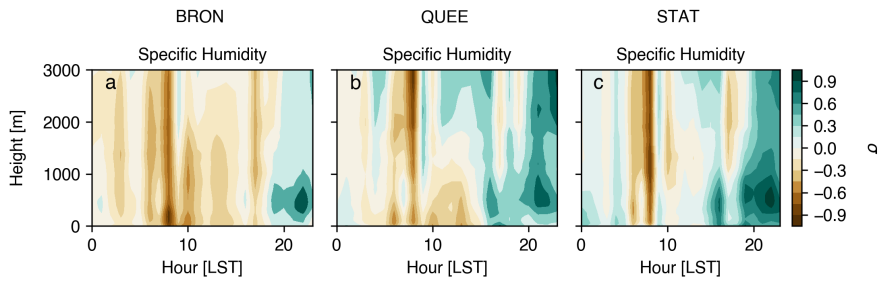


Figure 30: Anomalies of q for heat wave days with a sea breeze relative to heat wave days without a sea breeze.